Geophys. J. Int. (2007) **170,** 687–699 doi: 10.1111/j.1365-246X.2007.03412.x

Crustal thickness variations in the margins of the Gulf of California from receiver functions

Patricia Persaud,[1] Xyoli Pérez-Campos[2] and Robert W. Clayton[3]

[1] *Lamont-Doherty Earth Observatory of Columbia University, Palisades,* NY 10964*, USA*
[2] *Departamento de Sismología, Instituto de Geofísica, Universidad Nacional Autónoma de México, Ciudad Universitaria, Coyoacán, Mexico* D. F. 04510*, Mexico*
[3] *Seismological Laboratory, California Institute of Technology, Pasadena,* CA 91125*, USA. E-mail: clay@gps.caltech.edu*

Accepted 2007 February 16. Received 2006 December 22; in original form 2006 November 28

SUMMARY

Receiver functions (RFs) from teleseismic events recorded by the NARS-Baja array were used to map crustal thickness in the continental margins of the Gulf of California, a newly forming ocean basin. Although the upper crust is known to have split apart simultaneously along the entire length of the Gulf, little is known about the behaviour of the lower crust in this region. The RFs show clear *P*-to-*S* wave conversions from the Moho beneath the stations. The delay times between the direct *P* and *P*-to-*S* waves indicate thinner crust closer to the Gulf along the entire Baja California peninsula. The thinner crust is associated with the eastern Peninsular Ranges batholith (PRB). Crustal thickness is uncorrelated with topography in the PRB and the Moho is not flat, suggesting mantle compensation by a weaker than normal mantle based on seismological evidence. The approximately W–E shallowing in Moho depths is significant with extremes in crustal thickness of ∼21 and 37 km. Similar results have been obtained at the northern end of the Gulf by Lewis et al., who proposed a mechanism of lower crustal flow associated with rifting in the Gulf Extensional Province for thinning of the crust. Based on the amount of pre-Pliocene extension possible in the continental margins, if the lower crust did thin in concert with the upper crust, it is possible that the crust was thinned during the early stages of rifting before the opening of the ocean basin. In this case, we suggest that when breakup occurred, the lower crust in the margins of the Gulf was still behaving ductilely. Alternatively, the lower crust may have thinned after the Gulf opened. The implications of these mechanisms are discussed.

Key words: Moho depth, receiver functions, lower crustal flow

1 INTRODUCTION

Oblique rifts are abundant in the geological record. Examples are the modern Dead Sea-Gulf of Aqaba system and late Mesozoic Ivory Coast-Ghana margin (Wilson 1965). The Gulf of California, at the southern end of the Pacific–North America Plate boundary is a ∼1400 km long, highly sedimented, oblique rift characterized by long transform faults and short spreading centres (Londsdale 1989). It is one of the few places where the poorly understood process of continental breakup can be directly studied. Here, continental rifting began after a period of minor extension (e.g. Stock & Hodges 1989; Gans 1997; Nieto-Samaniego *et al.* 1999; Henry & Aranda-Gómez 2000; Ferrari *et al.* 2002) above a subduction-related volcanic arc (Gastil *et al.* 1979), which was supposedly oriented oblique to the extension direction. Current Pacific–North America Plate motion is taken up primarily by distributed faulting. This has been documented in the southern Gulf and on its margins (Fletcher & Munguía 2000), as well as in the northern one third of the Gulf, where multiple small-offset faults instead of throughgoing transform faults exist (Persaud *et al.* 2003). The diffuse nature of deformation, despite ∼6 Ma of fast spreading (5 cm yr^{-1} full rate), is curious and is manifested in the lack of organized seafloor spreading throughout the Gulf (Londsdale 1989). It is thought that wide rifts result from the extension of thick, hot crust when the mantle lithosphere is weak and the lower crust is weak, but not so weak that core complexes form (Buck 1991).

To help us understand the evolution of deformation at this plate boundary and what processes delay the transition to seafloor spreading, we seek to constrain the nature of the crust beneath the Gulf. Recent cross-Gulf tiepoints in the form of ∼255 km dextral offset of 6.3 Ma pyroclastic flow deposits (Oskin *et al.* 2001) support the exact fit of the rifted conjugate margins in the Upper Delfín Basin, with only a few tens of kilometres of dextral displacement occurring between 12.6 and 6.3 Ma (Oskin *et al.* 2001). On this basis, very little upper continental crust is expected beneath the Gulf at least not in this one basin segment. Basement rocks in the southern

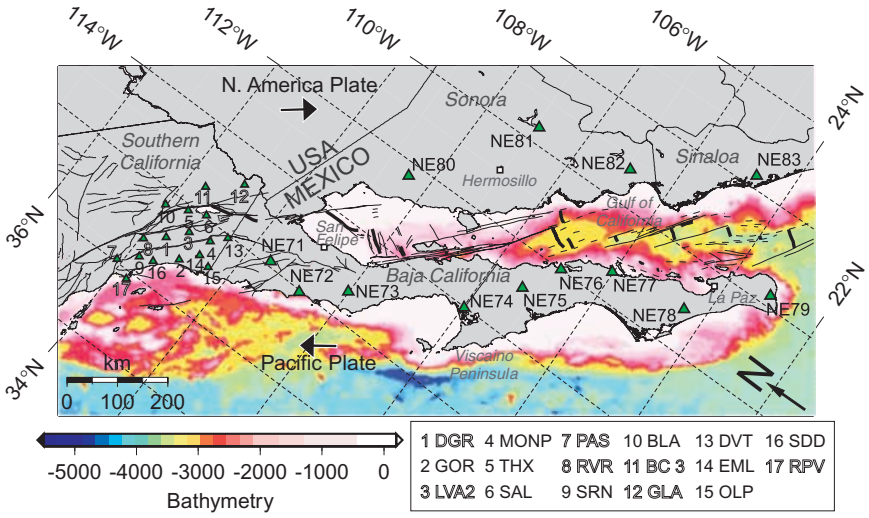

Figure 1. Map showing the major faults along the Pacific-North America plate boundary in southern California (Jennings 1994) and the Gulf of California (Fenby & Gastil 1991), and the station locations used in this study. Southern California stations are numbered according to the legend (bold text are stations that were also analysed by (Zhu & Kanamori 2000). See also Table 1). The 13 stations prefixed with NE are part of the NARS-Baja array. The bathymetry of the region is coloured and emphasizes the very shallow water depths in the northern Gulf. Thick black arrows indicate the current Pacific–North America relative Plate motion direction N37°W (Atwater & Stock 1998).

California and northern Baja California consist of the Jurassic–Cretaceous Peninsular Ranges batholith (PRB). The batholith is well exposed north of the Vizcaino peninsula in the Peninsular Ranges, which are part of a larger geologic province that extends to the tip of the Baja California peninsula (Oliver 1980; Lagenheim & Jachens, 2003; Fig. 1). Langenheim & Jachens (2003) used magnetic data to show that the western PRB extends along the full length of the peninsula, that is, ∼1200 km northwest from the southern tip of the peninsula. Their results lend support to the hypothesis of Stock & Hodges (1989), that since the opening of the Gulf, the Baja California peninsula (south of the Agua Blanca fault) has behaved as a rigid block. Langenheim & Jachens (2003) further proposed that the location of Gulf rifting was influenced by the mafic western PRB, which was stronger than the surrounding crust. Although no direct constraints on the degree of extension of the lower crust in the continental margins exist, three studies along a profile in northern Baja California found that the crust closer to the Gulf was thinner than the crust on the Pacific side of the peninsula. Ichinose *et al.* (1996), Lewis *et al.* (2000) and Lewis *et al.* (2001) explained this thinning as resulting from diffuse lower crustal extension in response to rifting in the Gulf Extensional Province, however, the timing of this extension remains unclear. Our purpose is, therefore, to examine the variation in crustal thickness in the continental margins around the entire Gulf of California and to use this information to suggest bounds on the amount of lower continental crust that could exist within the Gulf.

We estimate the variation of crustal thickness in Baja California and Sonora, Mexico, the continental margins of the Gulf of California using broad-band seismic data from the NARS-Baja network (Fig. 1) to calculate receiver functions (RFs). This technique has been widely used to map the depth to the Mohorovičić discontinuity (Moho) and the results can be interpreted in a fairly straightforward manner in areas of extension where the lithospheric structures are mainly flat-lying. Along with the inferences on the lower crustal composition beneath the Gulf, this study provides Moho depth estimates and V_p/V_s values for parts of Baja California and Sonora, Mexico, where the regional crustal thickness is only grossly known (e.g. Urrutia-Fucugauchi 1986). This study is now possible with the new data collected by the NARS-Baja network.

2 DATA

Starting in 2001, 18 broadband seismic stations were deployed, as part of the Network of Autonomously Recording Seismographs (NARS)-Baja network in Baja California and Sonora, Mexico (Clayton *et al.* 2004). The recordings from these stations provide a new dataset and a unique opportunity to map the crustal thickness on a regional scale around the entire Gulf of California. We use data from 13 NARS-Baja stations, 9 in Baja California and 4 in Sonora, along with 17 southern California stations (Fig. 1 and Table 1). The southern California stations were selected for an evenly spaced distribution from latitude 34° southward, as well as good data availability and quality within our time period. In this study, the RFs from the southern California stations are essentially used as a quality check on the RFs from the NARS-Baja network. We note that the data quality of the coastal stations is considerably poorer than that of the inland stations. Since published Moho depth estimates for southern California based on receiver function studies are largely confirmed by our work (Table 1), we do not analyse our results in southern California in detail. Instead, we focus on our results for the NARS-Baja stations. From an initial 399 teleseismic events with magnitudes above 5.9 M_w that occurred over a period of 27 months between 2002 April and 2004 August, we selected a total of 134 events (Fig. 2 and Table B1 in Appendix B). From these events, data for individual stations were selected if they met the following conditions: the event was located within a ∼30°–90° distance range and the *P* wave was readily identifiable (see data sample at two NARS-Baja stations in Fig. 3). The final distribution of events per station is shown in Fig. 4.

3 METHOD

Receiver functions are time series that provide us with an image of the earth structure close to the receiver. The technique involves the

Table 1. Stations used in teleseismic receiver function analysis.

Station	Latitude (°)	Longitude (°)	Altitude (m)	Events	Moho depth (km)	V_p/V_s
AZ.LVA2[a]	33.35160	−116.56150	1435.00	51	29.50 (29.10,29.90)	1.80 (1.79,1.81)
AZ.MONP	32.89270	−116.42250	1920.00	30	30.60 (30.00,31.40)	1.76 (1.74,1.79)
CI.BC3[b]	33.65484	−115.45309	1080.00	31	25.00 (24.60,25.40)	1.82 (1.79,1.84)
CI.BLA	34.06970	−116.38890	1214.00	43	31.00 (30.60,31.40)	1.86 (1.84,1.87)
CI.DGR[c]	33.64996	−117.00948	609.00	28	32.90 (32.50,33.40)	1.79 (1.78,1.81)
CI.DVT	32.65910	−116.10059	870.00	27	26.60 (26.10,27.10)	1.84 (1.81,1.86)
CI.EML	32.89083	−116.84566	131.00	37	31.40 (31.10,31.80)	1.90 (1.89,1.90)
CI.GLA[d]	33.05107	−114.82779	514.00	44	27.50(27.20,27.80)	1.68 (1.65,1.69)
CI.GOR	33.16000	−117.23000	46.00	23	38.90 (36.90,40.80)	1.66 (1.60,1.70)
CI.OLP	32.60783	−116.93036	130.00	19	28.80 (28.20,29.50)	1.79 (1.76,1.81)
CI.PAS[e]	34.14844	−118.17117	257.00	42	28.10 (27.50,29.60)	1.74 (1.70,1.76)
CI.RPV[f]	33.74329	−118.40426	64.00	21	28.90 (28.50,29.20)	1.61 (1.60,1.62)
CI.RVR[g]	33.99351	−117.37545	232.00	36	31.40 (31.00,32.00)	1.79 (1.77,1.81)
CI.SAL	33.27989	−115.98617	−22.00	14	20.50 (19.40,21.30)	1.61 (1.60,1.69)
CI.SDD	33.55259	−117.66171	85.00	16	29.20 (27.40,30.00)	1.90 (1.81,1.90)
CI.SRN	33.82843	−117.78938	181.00	22	28.90 (28.20,29.70)	1.81 (1.77,1.88)
CI.THX	33.63481	−116.16402	−44.00	5	22.90 (22.10,23.70)	1.62 (1.60,1.67)
NR.NE71[h]	31.68973	−115.90526	1155.00	61	33.70 (33.20,33.90)	1.80 (1.79,1.81)
NR.NE72[i]	30.84843	−116.05857	17.00	21	31.90 (31.20,32.50)	1.85 (1.82,1.88)
NR.NE73[j]	30.06510	−115.34847	489.00	10	37.50 (35.80,39.60)	1.81 (1.75,1.87)
NR.NE74[k]	28.00751	−114.01380	21.00	10	33.90 (32.40,35.40)	1.77 (1.70,1.82)
NR.NE75[l]	27.29334	−112.85649	137.00	56	27.60 (27.30,27.90)	1.79 (1.78,1.81)
NR.NE76[m]	26.88894	−111.99905	35.00	25	20.90 (20.50,21.40)	1.83 (1.80,1.85)
NR.NE77[n]	26.01577	−111.36133	40.00	32	23.70 (23.30,24.00)	1.80 (1.77,1.8)
NR.NE78[o]	24.39820	−111.10643	82.00	17	29.50 (28.20,31.00)	1.75 (1.71,1.79)
NR.NE79[p]	23.11937	−109.75611	225.00	27	25.80 (25.10,26.50)	1.70 (1.66,1.75)
NR.NE80[q]	30.50000	−112.31993	225.00	14	32.10 (30.80,33.40)	1.64 (1.60,1.68)
NR.NE81[r]	28.91834	−109.63626	295.00	17	28.10 (27.20,29.20)	1.74 (1.71,1.77)
NR.NE82[s]	26.91566	−109.23084	183.00	21	25.90 (25.40,26.50)	1.73 (1.71,1.76)
NR.NE83[t]	24.73088	−107.73933	28.00	2	20.30 (20.00,21.20)	1.76 (1.69,1.82)

Notes. [a]29.6 ± 0.9 km, 1.80 ± 0.05; [b]25.1 ± 1.6 km, 1.84 ± 0.09; [c]32. 8± 1.3 km, 1.80 ± 0.06; [d]27.0 ± 0.6 km, 1.72 ± 0.04; [e]28.0 ± 1.0 km, 1.73 ± 0.07; [f]21.5 ± 0.7 km, 1.84 ± 0.05; [g]30.7 ± 0.9 km, 1.83 ± 0.04; [h]Agua Blanca; [i]Camalu; [j]Turquesa; [k]Guerrero Negro; [l]San Ignacio; [m]Mulege; [n]Loreto; [o]Las Pocitas; [p]San Jose del Cabo; [q]Caborca; [r]Novillo; [s]Navajoa and [t]Navolato.

isolation of the local response from the source effects (Phinney 1964; Vinnik 1977). Rays ending in a *P*-leg that arrive at the receiver have more energy on the vertical component seismograms and than those ending in *S*-legs (Fig. A1). The vertical component seismograms are, therefore, used to enhance or isolate the *P*-to-*S* conversions that occur close to the receiver by deconvolving the vertical from the horizontal components. This technique produces crustal thickness estimates that are localized to a zone of approximately 15 km wide (assuming a 30-km crust).

For each event-station pair, data were selected within the distance ranges of 30°–90° and initially windowed 30 s before and 120 s after the *P*-wave pick. Only signals with a good signal-to-noise ratio and a clearly identifiable *P*-wave arrival were used. The records were rotated to the *Z*-vertical *R*-radial and *T*-transverse coordinate system, the trend and mean were removed, and a 5 per cent cosine taper was applied. The taper helps to reduce the noise in the deconvolution.

An additional rotation into *LQT* (a ray-based coordinate system) was carried out by finding the eigenvectors of the covariance matrix and minimizing the rotation (Vinnik 1977; Husebye *et al.* 1975; Kanasewich 1973; Appendix A). This is intended to focus the *P*-wave energy on the *L*-component, the *SV*-energy on the *Q* component and the *SH*-energy on the *T* component. Here it is important that gain is applied correctly to the signals and that the window over which the covariance is calculated contains the first few cycles of the *P* wave and no anomalous spikes.

Receiver functions can be modelled in either the frequency domain (Phinney 1964; Langston 1979; Owens *et al.* 1984) or time domain (Vinnik 1977); both require the deconvolution of the vertical component seismogram from the horizontal components. We found the results of both approaches very similar and chose the less CPU intensive frequency domain deconvolution. The *LQT* signals were then transformed into the frequency domain for the deconvolution; here the *Q* and *T* signals are each divided by the L signal. A waterlevel is first applied to the *L* signal to avoid division by zero and enhancement of noise (Clayton & Wiggins 1977). The possible waterlevel parameters considered were: 0.0001, 0.001, 0.01 and 0.1. The waterlevel is determined by adding a fraction (determined by the waterlevel parameter) of the maximum of the *L*-signal to the sample if the sample is below this value. After deconvolution the receiver functions were first filtered with a Gaussian filter before transformation back into the time domain. The width of the Gaussian filter used is either 2.5 or 5. The narrower filter width is used when the level of high-frequency noise in the RFs is high.

To determine the Moho depth for each station, we calculate the weighted sum of the amplitudes of each receiver function at *P-Pms*, *P-PmpPs* and either *P-PmpSs* or *P-PmsPs* travel times for a range of depths, H and V_p/V_s or κ values (Zhu & Kanamori 2000; Fig. 5). Zhu & Kanamori (2000) showed that the crustal thickness is not sensitive to crustal *P* velocity and that the uncertainty in both V_p/V_s and crustal thickness could be reduced significantly when the *Ps* wave arrival and its later multiples are stacked coherently. This

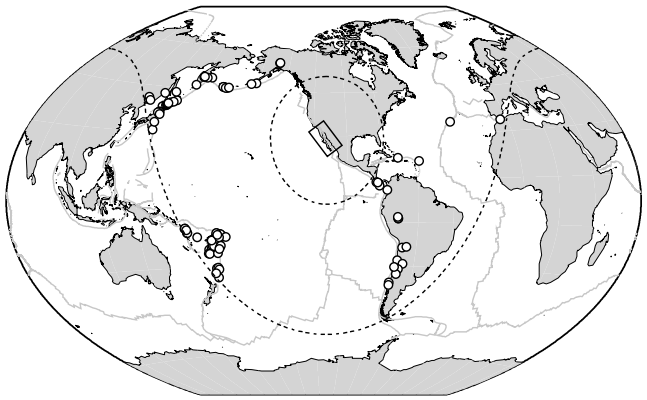

Figure 2. Map of showing the distribution of events used in the receiver function study. Map showing the distribution of the 134 events considered in this study. The black box marks the Gulf of California study area shown in Fig. 1. Dotted lines at distances of 30° and 90° away from the centre of the study area enclose the selected events.

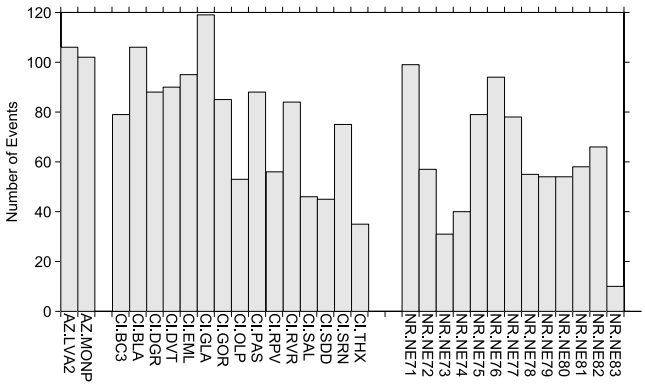

Figure 4. Histogram of events per station. Histogram showing the number of good quality records per station considered. RFs were calculated for all of these events, but only approximately 50 per cent of these events gave usable RFs. Note the number of good quality teleseismic records for the NARS-Baja stations is directly comparable to those for the stations in southern California, which were selected because they had high quality data.

approach uses the differential tau or difference in travel times between the *P* and *Ps* waves or reverberations as a 'moveout' correction before stacking in a plane-wave approximation, assuming a locally flat crust–mantle boundary. If this condition is not true, the result is usually an unclear maximum in the H-κ trade-off curve. The maximum of the H-κ stack gives an estimate of the crustal thickness and κ value. In this method, the average crustal V_p must be specified. The crustal thickness estimates scale linearly with this value. In this study, we have fixed the average V_p at 6.3 km s^{-1} for all stations, since we do not have independent estimates for individual stations. The uncertainties are calculated from the distribution of the maxima of the stacks of 200 bootstrap samples of the receiver functions. Simulated annealing was used to search for the maxima. The receiver functions shown here have been filtered for display purposes only, using a singular value decomposition filter after (Chevrot & Girardin 2000).

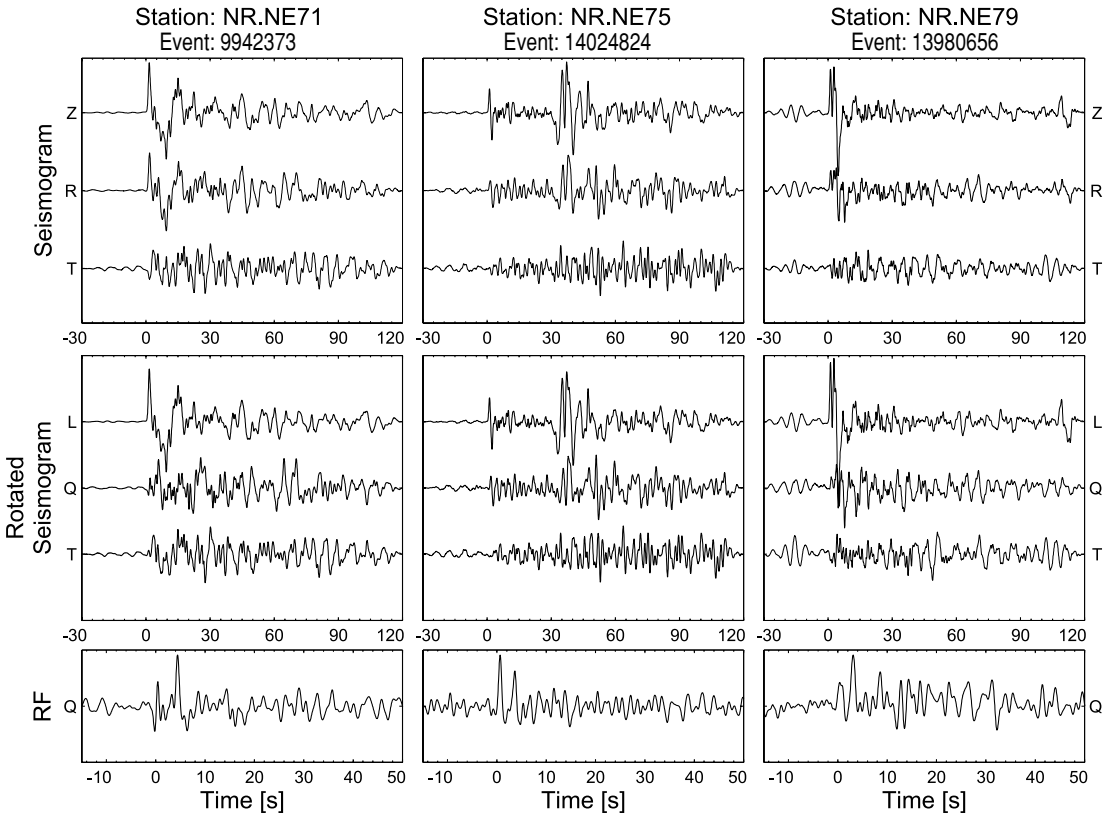

Figure 3. Data sample for stations NE71 (left), NE75 (centre), and NE79 (right). Upper panel shows the vertical, radial and transversal component; centre panel shows the *LQT* rotated signals and the bottom panel the corresponding radial component of the receiver function.

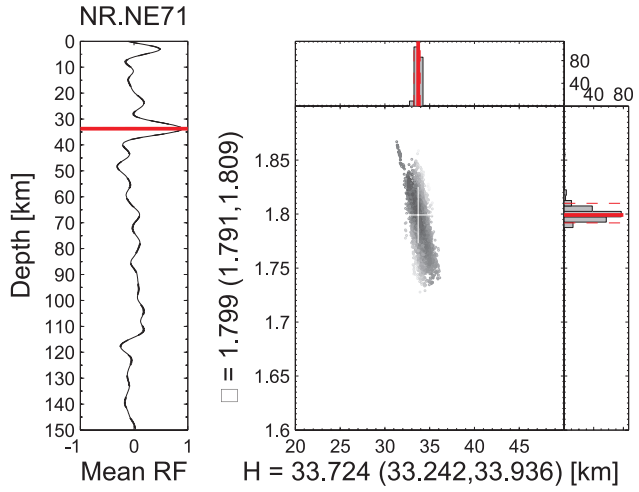

Figure 5. Example of H-κ domain stacking of receiver functions from NR.NE71. The left panel shows the mean RF plotted in depth versus normalized amplitude. The upper and lower limits of the 90 per cent confidence interval almost exactly coincide with the RF and are, therefore, barely visible at this scale. The red line marks the maximum determined by 200 bootstrap resamplings of the RFs and stacking in the H-κ domain (see text for details). The Moho P-to-S conversion is indicated. The right-hand panel shows the results of the stacking with the 90 per cent confidence interval marked in red.

4 DEPTH AND NATURE OF THE MOHO IN BAJA CALIFORNIA

In general, there is very little detectable azimuthal variation in Moho depth at individual stations. In the case of a 35 km thick crust and a near-vertical, 1 Hz incident S wave, the P-to-S conversions from the Moho sample a circle with a radius of ∼7 km around the station. Because of the natural bias in source regions, the events used in this study cluster both in backazimuth and epicentral distance. The NW and SW quadrants of backazimuth are very well sampled, whereas the SE is moderately sampled, and events from the NE are rare (Fig. 6). In the first 9 months of data, events from the NE were entirely absent and the SW and SE quadrants were poorly sampled. Epicentral distance ranges of ∼70°–90° are the most common. At these distances, the differential moveout of the Ps phase relative to the P is minimal. For these reasons, the expected changes in arrival time of the Ps on the radial RF due to a dipping Moho or the expected changes in the Ps amplitudes with changing backazimuth (Cassidy 1992) might go undetected, especially for shallow dips. Keeping these limitations in mind, we first examine the radial (Q) and transverse (T) receiver functions at and around the time of the P-to-S conversion from the Moho (Pms) and search for indications of anisotropic layers directly beneath the Moho.

Pms is easily identified in all of the RFs. In most cases, it appears as a single positive swing at around ∼2–5 s after the P arrival (Figs 7–10). In some instances, it is a composite pulse, made up of two positive swings, which arises from the interference with a P-to-S conversion from a shallow crustal layer that has a smaller relative moveout. The sharp one-sided nature of Pms indicates that the Moho is a sharp transition (Levin *et al.* 2002). However, in most cases, the presence of energy from Pms in the transverse RFs is an indication of anisotropy in the mantle beneath the Moho (Bostock 1997). This is particularly clear in the RFs in Figs 7 and 9, which leads to a possible interpretation of the Moho beneath these stations as the upper boundary of an anisotropic zone that is gradational beneath the Moho (Levin & Park 2000). Other evidence for anisotropy in the mantle is discussed below.

Using the H-κ stacking procedure, we stack all of the RFs for each station to determine the Moho depth. These values are shown with the corresponding error in Table 1. The poor quality of the RFs from station NE74 is likely due to its location near a semi-closed bay near the Vizcaino peninsula. The ringy nature of the data may thus be the result of seismic wave focusing related to the coastline geometry. Our Moho depth estimate of 34 km beneath this station is based on ten poor quality receiver functions but is similar to the

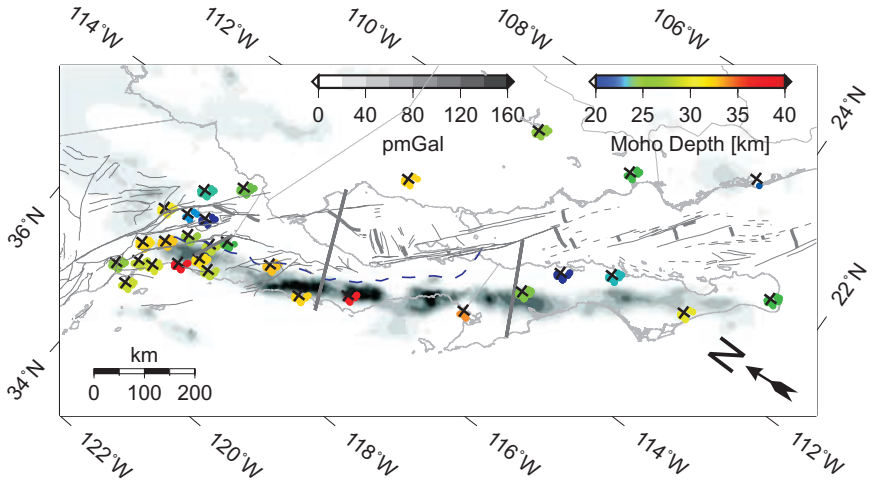

Figure 6. Map of crustal thickness in southern California, Sonora and Baja California, Mexico. Moho depths have been corrected for altitude and are relative to sea level. Crosses at the station locations indicate the four compass quadrants with the coloured dots indicating the Moho pierce points, assuming a Moho depth of 30 km and an IASP91 velocity model. See Fig. 1 for station names. Thick lines are the profiles shown in Fig. 11. The grid of magnetic potential (pseudogravity) from Langenheim & Jachens (2003) is shown to illustrate the existence of the western Peninsular Ranges batholith along the full length of the peninsula. Striped region marks the Gulf Extensional province as defined by Stock & Hodges (1989). Stations were projected onto B–B′ and shifted so that the station altitude would better fit the topography. See text for a discussion.

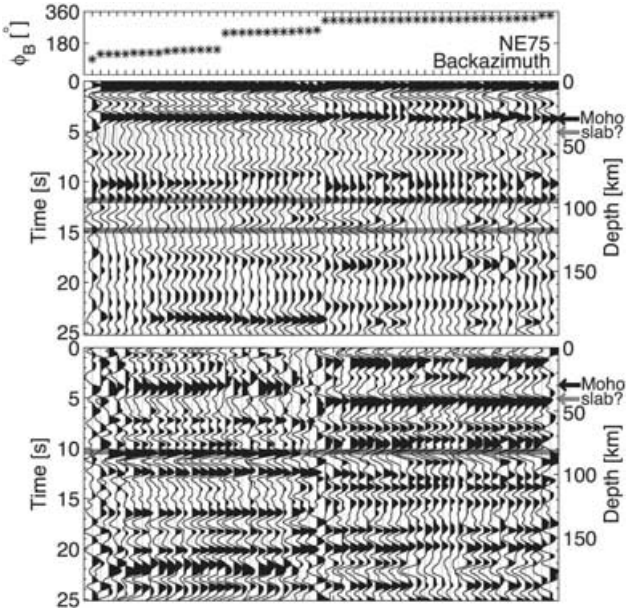

Figure 7. Q and T components of the receiver functions of NE75. The Q (middle) and T (bottom) components of the receiver functions of NR.NE75 are shown. The RFs are sorted by backazimuth as indicated in the top plot. Gray horizontal lines on the Q-components at 12 and 15 s mark the multiples discussed in the text. On the T-components the grey line at 10 s marks the evidence for anisotropy. The gray arrow points to evidence for a slab beneath this station. Crustal thickness is 27.6 km and V_p/V_s is 1.8.

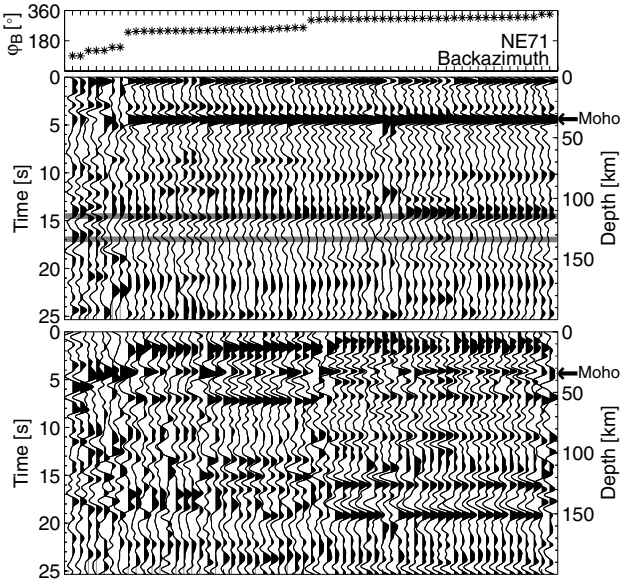

Figure 8. Q and T components of the receiver functions of NE71. The Q (middle) and T (bottom) components of the receiver functions of NR.NE71 are shown. The RFs are sorted by backazimuth as indicated in the top plot. Gray horizontal lines on the Q-components at 14 and 17.5 s mark the multiples discussed in the text. Crustal thickness is 33.7 km and V_p/V_s is 1.8.

value of 30 km reported in maps by Urrutia-Fucugauchi (1986). In contrast to NE74, NE71 has exceptionally good data quality. This is reflected in the tightness of the H and κ 90 per cent confidence interval (Fig. 5). The *Pms* is the most prominent arrival at around 4.5 s (33.7 km). The multiples from conversions at the Moho with positive and negative polarity arrive close to 14 and 17.5 s,

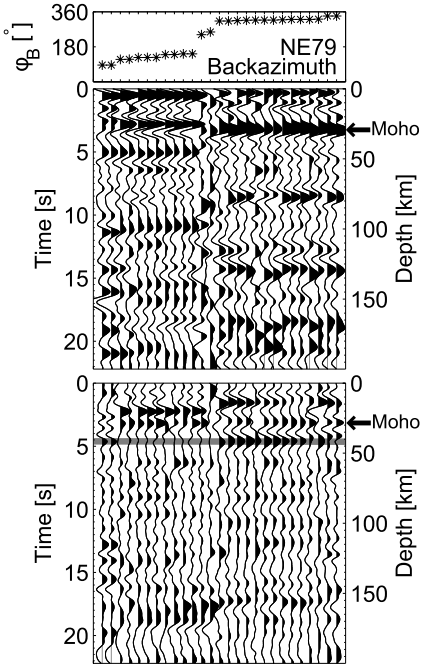

Figure 9. Q and T components of the receiver functions of NE79. The Q (middle) and T (bottom) components of the receiver functions of NR.NE79 are shown. The RFs are sorted by backazimuth as indicated in the top plot. The gray line on the T-components close to 5 s marks the evidence for anisotropy. Crustal thickness is 25.9 km and V_p/V_s is 1.7.

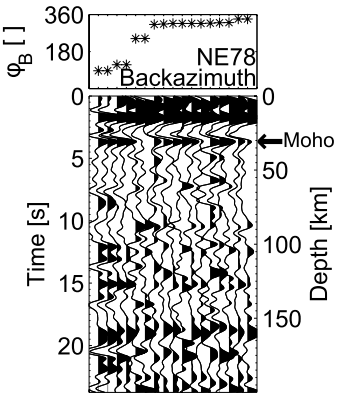

Figure 10. The Q component of the receiver functions of NR.NE78 is shown. The RFs are sorted by backazimuth as indicated in the top plot. Crustal thickness is 29.5 km and V_p/V_s is 1.7.

respectively, and are easily identifiable (Fig. 8). Similarly, the RFs from NE75 show a clear *Pms* arrival at around 3.5 s (27.6 km) with corresponding multiples at 12 and 15 s (Fig. 7). The polarity reversal of the multiple at 15 s may indicate a Moho with dip in the direction of incoming positively polarized multiples (Cassidy 1992). Based on this and the larger moveout with distance for the negative polarities, we conclude that the Moho beneath this station may have a shallow dip to the S–SE. A dipping Moho is also suggested for NE79 (Fig. 9), which is located at the tip of the peninsula. Note that arrivals from the west (backazimuth 180°–360°) show a narrower *Pms* compared to those from the east (backazimuth 0°–180°). If stacked separately, the corresponding crustal thicknesses are 31.7 and 27.7 km, respectively, with both backazimuth groups having low V_p/V_s, close to 1.6. We assume that there is some dip or at least

a step-like structure in the Moho beneath NE79. If, however, the broadening in the arrivals from the west is due to overlapping arrivals at the time of *Pms* and not just *Pms*, the Moho estimate of 27.7 km would be more robust.

The overall trend in crustal thickness is the crust closer to the Gulf is consistently thinner than the crust on the western side of the Baja California peninsula (Fig. 6). The thinner crust (21–26 km thick) is associated with stations NE76, NE77 and NE79, located in the southern half of the peninsula. Combining these results with those of Lewis *et al.* (2000) gives an ∼50 km wide zone of thin crust along the eastern peninsula. We map thicker crust (27–37 km) along the entire western side of the peninsula, based on our results from the other 6 peninsular stations.

5 MOHO DEPTHS IN SOUTHERN CALIFORNIA

Our estimates of the Moho depths in southern California range from 20 km for CI.SAL located in the Salton Trough to 39 km for CI.GOR located close to the coast on the western edge of the PRB (Fig. 6). A systematic variation in Moho depths can be noted from our results. The average crustal thickness to the west of the compositional boundary in the Peninsular Ranges of southern California is 33 km. This boundary was first identified by Gastil (1975), who separated the PRB into eastern and western zones based on structural and petrographic differences. Immediately to the east of the compositional boundary the crust is on average 28 km thick and closer to the Salton Sea crustal thickness averages 21 km.

Previously, Lewis *et al.* (2000) and Ichinose *et al.* (1996) have shown that the crust thins from west to east across the compositional boundary. Although we found a similar pattern of crustal thinning, the delay times of *Pms* for CI.EML, AZ.MONP and CI.DVT, our stations close to Ichinose *et al.* (1996) (profile A–A′, Fig. 11), are close and based on our estimates of crustal thickness, the crust appears to be thinned by only 4 km in this region and not 10 km over a lateral distance of 30 km as estimated by Ichinose *et al.* (1996). We do, however, note that their station density was much higher than ours. Furthermore, we do not expect this difference to be reduced considerably as a result of the particular constant V_p used. Since there is no standard velocity for the Gulf region, we chose to use a laterally invariant reference model so the results can be easily scaled to other models. This has become standard practice in regions where reference model exist (Zandt *et al.* 2004; Yan & Clayton 2006).

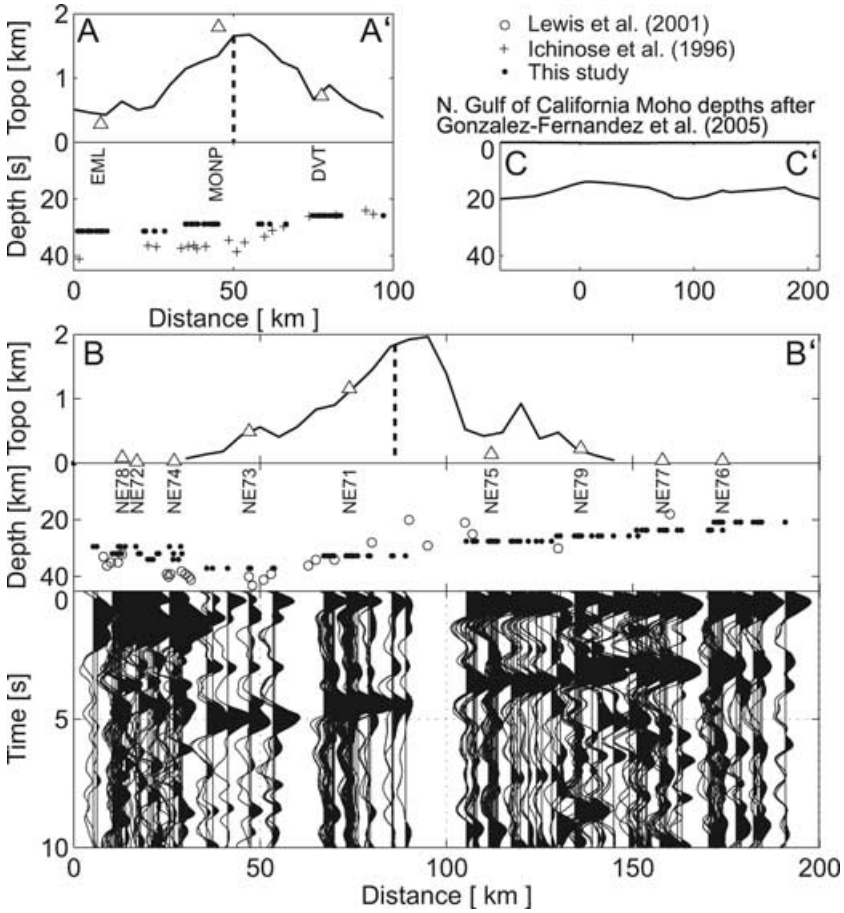

Figure 11. Profiles of receiver functions across the Baja California peninsula showing Moho depth variation. Profiles A–A′ after Ichinose *et al.* (1996) and B–B′ after Lewis *et al.* (2001) show Moho depths based on receiver function analysis. Dots in profile A–A′ are the projection of Moho depths from stations CI.EML, AZ.MONP and CI.DVT (this study); crosses are the results of Ichinose *et al.* (1996). Dots in profile B–B′ are the projection of Moho depths from nine NARS-Baja stations located in Baja California; open circles are the results of Lewis *et al.* (2001). Topography is shown in the top panel of A–A′ and B–B′. Profile C–C′ shows the offshore Moho depths in the northern Gulf after González-Fernández *et al.* (2005). Map view profile locations are shown in Fig. 6. Triangles are the station elevations; the dashed line indicates the compositional boundary approximated from magnetic potential (Langenheim & Jachens 2003; Fig. 6). The RFs were projected from their individual Moho pierce points, assuming a Moho depth of 30 km and an IASP91 velocity model.

The average crustal thickness is ∼28 km, which is similar to the results of another teleseismic receiver function study in southern California (Zhu & Kanamori 2000). In detail, however, their estimate of 28 km for PAS is 3.5 km thicker than ours and does not lie within the error bounds of our estimate, even though our Moho depths for the other six stations analysed in both studies match theirs very closely (Table 1). We attribute the difference at Pasadena to the choice of maxima particularly at close distances. Our method resulted in the first pulse of the doublet being chosen as the *Ps* conversion, while the choice of the later pulse would give a thicker crust and smaller V_p/V_s ratio as in the case of Zhu & Kanamori (2000). The doublet pulse for a shallow *Ps* conversion was previously interpreted as a shallow crustal discontinuity by Langston (1989) based on his effort to accept the deeper Moho depth estimate of 31 km by Hearn & Clayton (1986). Langston (1989), however, did note that the Moho could be no deeper than 27 km if the observed *Ps* conversion was indeed from the Moho.

6 OTHER RESULTS

Pre-Moho arrivals are likely due to layering in the crust or multiples from a crustal interface above the Moho. The first arrival on the *Q*-component is probably a shallow basin multiple, that is, a *P–SV* conversion from the base of the sediments like that observed by Kind *et al.* (1995). In almost all RFs, this arrival is the largest (e.g. Fig. 10) and has a delay time with respect to direct *P* of 0.5–1 s. This arrival is present in most radial RFs and also in some transverse RFs (e.g. Fig. 8), which suggests polarization of *P*-to-*S* conversion that produces *P*-to-*SH* energy. A low-velocity surface layer tends to broaden the direct *P*-arrival. Due to the high-velocity contrast, a *Ps* conversion also results from this layer. The absolute amplitudes of the RFs are very sensitive to near-surface high-velocity contrasts (Ammon 1991). This *Ps* phase arrives directly after the *P* and may not be resolvable in the conventional *ZRT* coordinate system (Cassidy 1992); however, the *LQT* rotation separates the direct *P*-arrival from the horizontal components, so that the *Ps* conversion from the shallow layer is resolvable.

Due to the lack of complete azimuthal coverage in the data, a thorough analysis for anisotropy is not possible here. We, however, briefly discuss the indications of anisotropic layers evident in the RFs. Arrivals below the Moho may give an indication of anisotropy since they show a polarity reversal on the *T*-component and have larger amplitudes than would be expected from a dipping layer (e.g. at ∼10 s in Fig. 7). Based on the apparently 180° symmetry in transverse energy at 10 s, for example, symmetry about the S and N backazimuths in the case of NE75, we assume that the anisotropic layer beneath this station has a horizontal symmetry axis polarized in a N–S direction (Savage 1998). Station NE76 is more complex, showing a polarity reversal at 10 s around 360° backazimuth, but no polarity reversal at 180° (based only on a single RF), however, an anisotropic layer similar to that beneath NE75 may exist here. A delay time of 10 s with respect to the *P*-arrival translates to ∼100 km depth; therefore, one explanation for these observations may be that the anisotropy is derived either by shearing at the base of the lithosphere or by preferential alignment of slab minerals (Obrebski & Castro 2006). Based on a similar reasoning, we suggest that an anisotropic layer exists directly beneath the Moho of NE79 (Fig. 9).

We have also found some evidence for a slab beneath NE75. The slab would be a remnant of the Farrallon plate which foundered 11 Ma when subduction ceased along Baja (Ferrari *et al.* 2002). The *T*-component RFs show a prominent arrival between 5 and 6 s that is either not clear in the *Q*-components or is polarity reversed (Fig. 7). A polarity reversal in the *Q*-components could be an indication of anisotropy, with the negative polarity in the *Q*-component being indicative of the slab top.

7 DISCUSSION AND CONCLUSIONS

Our crustal thickness estimates along the Baja California peninsula are summarized in Fig. 11. This is a projection of all of the RFs for stations NE71–NE79 (Fig. 1) from their estimated *P*-to-*S* conversion points (30 km depth based on the IASP91 model) onto a N60°E profile that crosses the peninsula (profile B–B′ in Fig. 6) with some of the RFs unavoidably extending into the Gulf. This clearly demonstrates that the continental crust in the margins of the Gulf of California is thinnest closer to the Gulf. Similar results have been obtained in the Peninsular Ranges in southern California (Ichinose *et al.* 1996) (A–A′ in Fig. 6) and northern Baja California (Lewis *et al.* 2001) (B–B′ in Fig. 6). These authors propose a mechanism of diffuse lower crustal extension for thinning of the crust and suggest that the thinned crust is the eastern PRB and the thicker crust is the stronger, more mafic, western PRB. They propose that the change in crustal thickness is associated with a 'compositional' boundary between the two batholiths (Ichinose *et al.* 1996; Lewis *et al.* 2001). This 'compositional' boundary has only been mapped in the northern half of the peninsula where the batholith is exposed (Gastil *et al.* 1990). Recently, Langenheim & Jachens (2003) proposed that the location of Gulf rifting was influenced by the mafic western PRB, which was stronger than the surrounding crust. They suggested that the pattern of crustal thinning observed to the north by Lewis *et al.* (2001) may also extend the full length of the peninsula. This suggestion is supported by our large-scale observations of thinner crust along the eastern peninsula, likely associated with the eastern PRB and thicker crust along the western peninsula associated with the western PRB. The implications of these results are discussed below.

From our results and assuming an original crustal thickness of ∼35 km (similar to the western PRB) the eastern PRB appears to have been stretched by a factor of ∼2 or extended by 85 per cent if it was all thinned uniformly. Note that we define the eastern PRB to also include the Gulf Extensional Province defined by Stock & Hodges (1989), which extends in a thinner belt along the eastern Baja California peninsula (Fig. 6). It is not unlikely, but cannot be proved here, that this pervasive thinning of the crust may have occurred in the Miocene, before the opening of the Gulf. In the margins of the Gulf, possible values of upper crustal extension in the late Miocene range from 80 to 90 per cent, with varying amounts of total extension possible throughout the Gulf Extensional Province (Stock & Hodges 1989). This extension was ENE directed and similar in structural style to extension in the Basin and Range province (Stock & Hodges 1989. Although more detailed mapping is needed before an accurate estimate of the total post-mid Miocene upper crustal extension can be made, local values range from 5 to 50 per cent (Stock & Hodges 1989). Thus, more extension may have occurred in the lower crust of the eastern PRB than the upper crust.

Two possible mechanisms exist for pervasive thinning of the lower crust with little extension of the upper crust: lower crustal flow and 'oceanization' of continental crustal blocks. Lower or mid-crustal flow has been suggested as a mechanism for maintaining a smooth Moho topography in the Basin and Range where thickened crust is thinned usually as a result of surface topography-related

pressure gradients to accommodate regional extension (Block & Royden 1990; Kruse *et al.* 1991). Lower crustal flow is, however, only likely when the crustal thickness exceeds 20 or 25 km and is accompanied by uplift and significant tilting without faulting (McKenzie *et al.* 2000). For the viscosity of the lower crust to be low enough for flow, the heat flow is expected to be higher than the continental average. Based on only sparse measurements, the heat flow values for the Baja California peninsula range from 42 to 84 mW m^{-2} (Urrutia-Fucugauchi 1986). Alternatively, shear within the continental crust may decrease the viscosity of the lower crust and facilitate flow as has also been proposed for the Dead Sea basin, where the heat flow is 45–54 mW m^{-2}, close to the continental average (Al-Zoubi & ten Brink 2002). This mechanism for facilitating flow in the lower crust would only apply if the eastern PRB was thinned after the Gulf opened and major transform faults started to develop. Whether shear- or topography-related, lower crustal flow acts to smooth out variations in crustal thickness, which implies that if the lower crust of the eastern PRB did flow, the flow was eastward, and the western PRB was not involved. Evidence for lower crustal flow within the Gulf itself is provided by wide angle refraction results that show large changes in the thickness of the lower crust relative to smaller variations in the overall crust (González-Fernández *et al.* 2005) (profile C–C′ in Fig. 11).

Crustal thickness along the Baja California peninsula appears to be uncorrelated with topography (Fig. 11; Lewis *et al.* 2001). Non-Airy type compensation as in the case of the southern Sierra Nevada (Wernicke *et al.* 1996) is supported. The Moho beneath the Peninsular Ranges is, however, not flat nor is the crustal thickness anticorrelated with crustal density. Because the lower-density eastern PRB is thinner than the higher-density western PRB, a Pratt-type root as suggested for the southern Sierra Nevada can be ruled out. Instead, Lewis *et al.* (2001) suggest compensation by upper mantle density variation or the flexural rigidity of the lithosphere supports the load of the eastern PRB. Seismic observations show that *P*-waves travelling through the upper mantle beneath the Gulf are 5–10 per cent slower than normal (Thatcher & Brune 1971) and S-wave velocity in the uppermost 200 km of the upper mantle is 6–8 per cent slower than in the PREM model (e.g. Ritsema & van Heijst 2000). Therefore, our preferred choice is compensation by density variations in the upper mantle. This does not require lower crustal flow, rather it allows for thinning of both the crust and mantle with no decoupling in the lower crust, therefore, in the Woodlark basin, Papua New Guinea, where the overall crust is thin beneath areas of the greatest surface extension (Abers *et al.* 2002). The Moho is indeed not flat in this region, and compensation is accomplished through mantle buoyancy and not crustal thickening (Abers *et al.* 2002).

Another mechanism for thinning the crust is through the 'oceanization' of crustal blocks. This has been reported from the Gulf of Guinea, where the ghost of tilted fault blocks is still seen beneath the reflection Moho (Rosendahl *et al.* 1992). The 'oceanization' of continental fault blocks is a gradual process and involves the progressive lateral replacement of continental fault blocks with oceanic crust. The reflection Moho marks the transition to a more ductile regime at depth. The implications of lower crustal flow versus 'oceanization' of continental fault blocks are significant, since the latter requires that thinning occurred after the Gulf opened and no continental crust would be expected within the Gulf. The view of lower crustal flow allows for the presence of continental crust within the Gulf and thus inherently weaker crust there. The question then is: was the middle or lower continental crust behaving ductilely as the Gulf opened?

Presumably, the eastern PRB had a thickness closer to that of the western PRB, that is, ∼40 km, before any Gulf-related extension began (Schmidt 2000). If the eastern PRB underwent 100 per cent of pre-Gulf extension, then its thickness at the opening of the Gulf was 20 km and the lower limit of the strain rate is 10^{-15} s^{-1}, assuming a 12–6 Ma period of stretching. Since the Gulf opened above a volcanic arc, the geotherm was probably elevated in the eastern PRB at the time. A comparison with the 'young lithosphere' stretching model of Pérez-Gussinyé *et al.* (2001) gives some insight into the conditions at final breakup. The young lithosphere model is based on the Woodlark basin, Papua New Guinea, where rifting of hot thick crust at high strain rates, 10^{-14} s^{-1} produced a narrow ocean-continent transition and lower crust that was still behaving ductilely at breakup (Pérez-Gussinyé *et al.* 2001 and references therein). We note that this model is for uniform pure shear of the entire crust, which limits its direct application to the eastern PRB, where the amount of the surface extension occurring before 6 Ma was probably not 100 per cent (e.g. Henry & Aranda-Gómez 2000) Based on this model, it is likely that at breakup, the lower crust in the continental margins of the Gulf, like that in the Woodlark basin, was still behaving ductilely, and as a result, some lower continental crust may exist within the current Gulf.

In summary, we have shown that overall the crust is thinnest (21–26 km) in a strip no wider than 50 km along the eastern Baja California peninsula and that this coincides with the eastern PRB and includes the Gulf Extensional Province. The western PRB is thicker (32–37 km) and may indeed have behaved as a rigid block during the opening of the Gulf. It is possible that extension of the eastern PRB (including the Gulf Extensional Province) may have occurred during the Miocene before the Pacific–North America Plate boundary was fully located in the Gulf of California. The timing of this extension is important for understanding the mechanism of thinning and its relationship to the current Gulf. If the eastern PRB was thinned after the Gulf opened by lower crustal flow then the amount of lower continental crust within the Gulf may be significant.

ACKNOWLEDGMENTS

We thank Gene Ichinose and Harold Magistrale for providing us with the results from Ichinose *et al.* (1996) and Lewis *et al.* (2001), respectively, and Victoria Langenheim for providing the magnetic potential results from Langenheim & Jachens (2003). Supported by NSF grants EAR-0111650. Contribution no. 8974, Division of Geological and Planetary Sciences, California Institute of Technology. Partial funding for X. Pérez-Campos from UNAM-PAPIIT grants IX1210004 and IN119505–3.

REFERENCES

Abers, G.A., Ferris, A., Craig, M., Davies, H., Lerner-Lam, A.L., Mutter, J.C. & Taylor, B., 2002. Mantle compensation of active metamorphic core complexes at Woodlark Rift in Papua New Guinea, *Nature,* **418,** 862–865.

Al-Zoubi, A. & ten Brink, U., 2002. Lower crustal flow and the role of shear in basin subsidence: an example from the Dead Sea basin, *Earth planet. Sci. Lett.,* **199,** 67–79.

Ammon, C.J., 1991. The isolation of receiver effects from teleseismic P waveforms, *Bull. seism. Soc. Am.,* **81**(6), 2504–2510.

Atwater, T. & Stock, J., 1998. Pacific-North America Plate Tectonics of the Neogene Southwestern United States: An Update, *Int. Geology Rev.,* **40,** 375–402.

Block, L. & Royden, L.H., 1990. Core complex geometries and regional scale flow in the lower crust, *Tectonics,* **9**(4), 557–567.

Bostock, M.G., 1997. Anisotropic upper-mantle stratigraphy and architecture of the Slave craton, *Nature,* **390,** 392–395.

Buck, W.R., 1991. Modes of continental lithospheric extension, *J. geophys. Res.,* **96,** 20 161–20 178.

Cassidy, J.F., 1992. Numerical experiments in broadband receiver function analysis, *Bull. Seism. Soc. Am.,* **82**(3), 1453–1474.

Chevrot, S. & Girardin, N., 2000. On the detection and identification of converted and reflected phases from receiver functions, *Geophys. J. Int.,* **141,** 801–808.

Clayton, R.W. & Wiggins, R.A., 1976. Source shape estimation and deconvolution of teleseismic bodywaves, *Geophys. J. R. astr. Soc.,* **47,** 151–177.

Clayton, R.W. *et al.*, 2004. The NARS-Baja seismic array in the Gulf of California rift zone, *MARGINS Newslett.,* **13,** 1–4.

Fenby, S.S. & Gastil, R.G., 1991. Geologic-tectonic map of the Gulf of California and surrounding areas, in *The Gulf and Peninsular Provinces of the Californias,* , pp. 79—83, eds. J.P. Dauphin & B.R.T. Simoneit, *Am. Assoc. Petroleum Geologists Memoir* 47.

Ferrari, L., López-Martínez, M. & Rosas-Elguera, J., 2002. Ignimbrite flare-up and deformation in the southern Sierra Madre Occidental, western Mexico: implications for the late subduction history of the Farallon plate, *Tectonics,* **21,** 10.1029/2001TC001302.

Fletcher, J.M. & Munguía, L., 2000. Active continental rifting in southern Baja California, Mexico: Implications for plate motion partitioning and the transition to seafloor spreading in the Gulf of California, *Tectonics,* **19**(6), 1107–1123.

Gans, G., 1997. Large-magnitude Oligo-Miocene extension in southern Sonora: Implications for the tectonic evolution of northwest Mexico, *Tectonics,* **16**(3), 388–408.

Gastil, G., Diamond, J., Knaack, C., Walawender, M., Marshall, M., Boyles, C. & Chadwick, B., 1990. The problem of the magnetite/ilmenite boundary in southern and Baja California, *Geolog. Soc. Am. Memoir,* **174,** 19–32.

Gastil, R.G., 1975. Plutonic zones in the Peninsular Ranges of southern California and northern Baja California, *Geology,* **3,** 361–363.

Gastil, R.G., Krummenacher, D. & Minch, J., 1979. The record of Cenozoic volcanism around the Gulf of California, *Geolog. Soc. Am. Bull.,* **90,** 839–857.

González-Fernández, A., Dañobeitia, J.J., Delgado-Argote, L.A., Michaud, F., Córdoba, D. & Bartolomé, R., 2005. Mode of extension and rifting history of upper Tiburón and upper Delfín basins, northern Gulf of California, *J. geophys. Res.,* **110,** doi:10.1029/2003JB002941.

Hearn, T.M. & Clayton, R.W., 1986. Lateral velocity variations in southern California I, Results from the upper crust from Pg waves, *Bull. seismol. Soc. Am.,* **76,** 495–509.

Henry, C.D. & Aranda-Gómez, J.J., 2000. Plate interactions control middle-late Miocene, proto-Gulf and Basin and Range extension in the southern Basin and Range, *Tectonophysics,* **318,** 1–26.

Husebye, E.S., Christoffersson, A. & Frasier, C.W., 1975. Orthogonal representations of array-recorded short period P-waves, *NATO ASI Series, Series E: Applied Sciences, no. 11, Exploitation of Seismograph Networks, Nordhoff* , Leiden, pp. 297–309.

Ichinose, G., Day, S., Magistrale, H. & Prush, T., 1996. Crustal thickness variations beneath the Peninsular Ranges, southern California, *Geophys. Res. Lett.,* **23**(22), 3095–3098.

Jennings, C.W., 1994. Fault activity map of California and adjacent areas, *California Division of Mines and Geology, California Geologic Data Map Series, Map No. 6, scale 1:750,000*.

Kanasewich, E.R., 1973. *Time Sequence Analysis in Geophysics*, The University of Alberta Press., 364 pp.

Kind, R., Kosarev, G.L. & Petersen, N.V., 1995. Receiver functions at the stations of the German Regional Seismic Network GRSN, *Geophys. J. Int.,* **121,** 191–202.

Kruse, S., McNutt, M., Phipps-Morgan, J. & Royden, L., 1991. Lithospheric extension near Lake Mead, Nevada: A model for ductile flow in the lower crust, *J. geophys. Res.,* **96**(B3), 4435–4456.

Langenheim, V.E. & Jachens, R.C., 2003. Crustal structure of the Peninsular Ranges batholith from magnetic data: Implications for Gulf of California rifting, *Geophys. Res. Lett.,* **30**(11), 1597, doi:10.1029/2003GL017159.

Langston, C.A., 1979. Structure under Mount Rainier, Washington, inferred from teleseismic body waves, *J. geophys. Res.,* **84**(B9), 4749–4762.

Langston, C.A., 1989. Scattering of teleseismic body waves under Pasadena, California, *J. geophys. Res.,* **94**(B2), 1935–1951.

Levin, V. & Park, J., 2000. Shear zones in the Proterozoic lithosphere of the Arabian Shield and the nature of the Hales discontinuity, *Tectonophysics,* **323**, 131–148.

Levin, V., Margheriti, L., Park, J. & Amato, A., 2002. Anisotropic seismic structure of the lithosphere beneath the Adriatic coast of Italy constrained with mode-converted body waves, *Geophys. Res. Lett.,* **29**(22), 2058.

Lewis, J.L., Day, S.M., Magistrale, H., Eakins, J. & Vernon, F., 2000. Regional crustal thickness variations of the Peninsular Ranges, southern California, *Geology,* **28**(4), 303–306.

Lewis, J.L. *et al.*, 2001. Crustal thickness of the Peninsular Ranges and Gulf Extensional Province in the Californias, *J. geophys. Res.,* **106**(B7), 13 599–13 611.

Lonsdale, P., 1989. Geology and tectonic history of the Gulf of California, in *The Eastern Pacific Ocean and Hawaii,* eds. D. Hussong, E.L. Winterer & R.W. Decker, Vol. N of The Geology of North America, pp. 499–522, Geological Society of America Boulder, CO.

McKenzie, D., Nimmo, F., Jackson, J.A., Gans, P.B. & Miller, E.L., 2000. Characteristics and consequences of flow in the lower crust, *J. geophys. Res,*, **105**(B5), 11 029–11 046.

Nieto-Samaniego, A.F., Ferrari, L., Alaniz-Alvarez, S.A., Labarthe-Hernández, G. & Rosas-Elguera, J., 1999. Variation of Cenozoic extension and volcanism across the southern Sierra Madre Occidental volcanic province, Mexico, *GSA Bull.,* **111**(3), 347–363.

Obrebski, M. & Castro Escamilla, R., 2006. Estudio de la estructura anisotropa de la corteza en el norte de Baja California y Sonora, México mediante observaciones de ondas convertidas *Ps*, UGM Reunión anual 2006, *GEOS,* **26** (1).

Oliver, H.W., 1980. Peninsular ranges, in *Interpretation of the Gravity Map of California and its Continental Margin,* California Division of Mines and Geology Bulletin, Vol. **205**, pp. 17–19.

Oskin, M., Stock, J. & Martin-Barajas, A., 2001. Rapid localization of Pacific-North America plate motion in the Gulf of California, *Geology,* **29**(5), 459–462.

Owens, T.J., Zandt, G. & Taylor, S.R., 1984. Seismic evidence for an ancient rift beneath the Cumberland Plateau, Tennessee: A detailed analysis of broadband teleseismic P waveforms, *J. geophys. Res.,* **89**(B9), 7783–7795.

Pérez-Gussinyé, M., Reston, T.J. & Phipps Morgan, J., 2001. Serpentinization and magmatism during extension at non-volcanic margins: the effect of initial lithospheric structure, in *Non-Volcanic Rifting of Continental Margins: A Comparision of Evidence from Land and Sea*, Vol. 187, pp. 551–576, eds. R.C.L. Wilson, R.B. Whitmarsh, B. Taylor & N. Froitzheim, Geological Society Special Publications.

Persaud, P., Stock, J.M., Steckler, M.S., Martin-Barajas, A., Diebold, J.B., González-Fernández, A. & Mountain, G.S., 2003. Active deformation and shallow structure of the Wagner, Consag and Delfín Basins, Northern Gulf of California, Mexico, *J. geophys. Res.,* **108**(B7), 2355, doi:10.1029/2002JB001937.

Phinney, R.A., 1964. Structure of the earth's crust from spectral behavior of long-period body waves, *J. geophys. Res.,* **69**(14), 2997–3017.

Ritsema, J. & van Heijst, H., 2000. New seismic model of the upper mantle beneath Africa, *Geology,* **28**(1), 63–66.

Rosendahl, B.R., Meyers, J., Groschel, H. & Scott, D., 1992. Nature of the transition from continental to oceanic crust and the meaning of reflection Moho, *Geology,* **20**, 721–724.

Savage, M.K., 1998. Lower crustal anisotropy or dipping boundaries? Effects on receiver functions and a case study in New Zealand, *J. Geophys. Res.,* **103**(B7), 15 069–15 087.

Schmidt, K., 2000, Investigation of arc processes: Relationships among deformation, magmatism, mountain building, and the role of crustal anisotropy in the evolution of the Peninsular Ranges batholith, Baja California, *PhD thesis*, University of Southern California.

Stock, J.M. & Hodges, K.V., 1989. Pre-Pliocene extension around the Gulf of California and the transfer of Baja California to the Pacific plate, *Tectonics,* **8,** 99–115.

Thatcher, W. & Brune, J.N., 1971. Seismic study of an oceanic ridge earthquake swarm in the Gulf of California, *Geophys. J. R. Astr. Soc.,* **22,** 473–489.

Urrutia-Fucugauchi, J., 1986. Crustal thickness, heat flow, arc magmatism, and tectonics of Mexico-preliminary report, *Geofisica Int.,* **25**(4), 559–573.

Vinnik, L.P., 1977. Detection of waves converted from P to SV in the mantle, *Phys. Earth planet. Interior,* **15,** 39–45.

Wernicke, B. *et al.*, 1996. Origin of high mountains in the continents: the Southern Sierra Nevada, *Science,* **271,** 190–193.

Wilson, J.T., 1965. A new class of faults and their bearing on continental drift, *Nature,* **207,** 343–347.

Yan, Z. & Clayton, R., 2007. Regional mapping of the crustal strcture in Southern California from receiver functions, *J. geophys. Res.,* in press.

Zandt, G., Gilbert, H., Owens, T.J., Duces, M., Saleeby, J. & Jones, C.H., 2004. Active foundering of a continental arc root beneath the southern Sierra Nevada in California, *Nature,* **431,** 41–36.

Zhu, L. & Kanamori, H., 2000. Moho depth variation in southern California from teleseismic receiver functions, *J. Geophys. Res.,* **105**(B2), 2969–2980.

APPENDIX A: ROTATION FROM ZRT TO LQT COORDINATE SYSTEM

The following steps were used to rotate the Z (Vertical), R (Radial) and T (Transverse) components of the seismograms to the corresponding L, Q and new T components. This method is based on that of Kanasewich (1973). First the covariance, that is, the products of the deviations from the means is calculated in 1 s windows centred at every time point, $t_j (j = 1, 2, \ldots, M)$ in a larger 30 s window around the P-wave arrival time. We therefore, consider a time window of length $N\Delta t$, M times; where N the number of time points in the window, and Δt is the sampling interval. Here, $N\Delta t = 1$ and $M = 30$. The mean, μ_1, of N observations of $X_{1i} (i = 1, 2, \ldots, N)$ is given by

$$\mu_1 = \frac{1}{N}\sum_{i=1}^{N} X_{1i}. \tag{A1}$$

The covariance between N observations of X_1 and X_2 is

$$\mathrm{Cov}\,[X_1, X_2]] = \frac{1}{N}\sum_{i=1}^{N} (X_{1i} - \mu_1)(X_{2i} - \mu_2). \tag{A2}$$

Considering the Z, R and T components, the covariance matrix is given by

$$V = \begin{pmatrix} \mathrm{Var}\,[R] & \mathrm{Cov}\,[R, T] & \mathrm{Cov}\,[R, Z] \\ \mathrm{Cov}\,[R, T] & \mathrm{Var}\,[T] & \mathrm{Cov}\,[T, Z] \\ \mathrm{Cov}\,[R, Z] & \mathrm{Cov}\,[T, Z] & \mathrm{Var}\,[Z] \end{pmatrix}, \tag{A3}$$

where Var is the autocovariance or variance, for example, Cov[X_1, X_1], and Cov is the covariance as defined in eq. (A2). Evaluating V, M times, results in a matrix, Q, with the dimensions ($3 \times 3 \times M$) given by

$$Q = V(t_j), \tag{A4}$$

where $V(t_j)$ is V evaluated as in eq. (A4) at the points $t_j (j = 1, 2, \ldots, M)$. We take the average of Q along the third dimension to minimize the influence of anomalous spikes, thus reducing the Q matrix to a 3×3 matrix, W as follows

$$W = \frac{1}{M}\sum \begin{pmatrix} Q\,(1, 1, j) & Q\,(1, 2, j) & Q\,(1, 3, j) \\ Q\,(2, 1, j) & Q\,(2, 2, j) & Q\,(2, 3, j) \\ Q\,(3, 1, j) & Q\,(3, 2, j) & Q\,(3, 3, j) \end{pmatrix}. \tag{A5}$$

The eigenvalues of W are λ_1, λ_2 and λ_3, where λ_1 represents the largest eigenvalue and λ_3 represents the smallest eigenvalue. The corresponding eigenvectors are $\mathbf{e}_1$, $\mathbf{e}_2$ and $\mathbf{e}_3$. In an ideal case, the transformation matrix for the rotation into the LQT coordinate system is $[\mathbf{e}_1; \mathbf{e}_2; \mathbf{e}_3]$, and the transformation is carried out as follows

$$\begin{pmatrix} L \\ Q \\ newT \end{pmatrix} = \begin{pmatrix} \mathbf{e}_1 \\ \mathbf{e}_2 \\ \mathbf{e}_3 \end{pmatrix} \begin{pmatrix} Z \\ R \\ T \end{pmatrix}. \tag{A6}$$

This rotation can be problematic since the $\mathbf{e}_1$, $\mathbf{e}_2$ and $\mathbf{e}_3$ eigenvectors do not necessarily always explain decreasing variance in the data. We have found that the variance often fails to provide a reasonable rotation of the data and have, therefore, used the maximum component of the eigenvector to determine which new axes that eigenvector best explains. We have also found that two instead of three eigenvectors will in a small number of cases sufficiently explain the data. This ambiguity is then resolved by using the eigenvalues. After the rotation the Q and T components are shifted 15 s forward in time with respect to the L component by clipping 15 s of pre P wave noise from the beginning of the L component and 15 s from the end of the Q and T signals. The clipped ends of the signals are tapered. The Q and T components are conceptually the convolved signals, therefore, applying this time-shift before the deconvolution allows for 15 s of pre P-wave noise at the beginning of the deconvolved receiver function. The level of this pre-signal noise is low for stable deconvolutions.

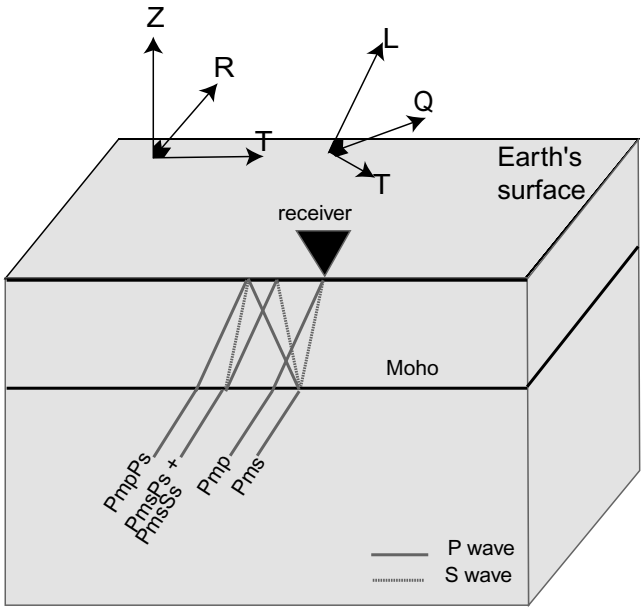

Figure A1. Ray diagram showing *ZRT* to *LQT* rotation. Schematic drawing showing the *ZRT* and *LQT* coordinate systems. Ray conversions at the Moho and multiples are discussed in the text.

APPENDIX B: LOCATIONS AND MAGNITUDES OF EVENTS USED IN TELESEISMIC RECEIVER FUNCTION ANALYSIS

Table B1. Locations and magnitudes of events used in teleseismic receiver function analysis

Event ID	Latitude (°)	Longitude (°)	Depth (km)	M_w
9777469	−14.4000	167.6000	10.00	5.90
12880392	16.9000	−100.8000	33.00	6.10
12880404	−27.3000	−70.0000	61.00	6.60
12880408	−16.4000	173.2000	33.00	5.90
12881052	13.1000	144.5000	76.00	7.20
12895912	−17.8000	−178.8000	527.00	5.80
13115436	−17.9000	−174.6000	131.00	6.30
13359428	53.9000	−161.3000	33.00	6.00
13487432	−28.9000	−66.6000	21.00	6.00
13657276	−47.8000	99.7000	10.00	6.10
13658260	8.7000	−83.9000	33.00	6.20
13658244	−17.8000	−178.7000	564.00	5.90
9792597	−12.6000	166.3000	33.00	6.70
9792721	−30.8000	−70.9000	52.00	6.50
9793833	35.7000	48.9000	10.00	6.30
9795473	−7.0000	103.9000	10.00	6.40
9795905	43.8000	130.7000	566.00	7.20
9800261	−12.4000	166.5000	33.00	6.20
9796365	−22.1000	179.1000	620.00	6.10
9799465	43.6000	−127.2000	10.00	5.90
9804941	8.1000	−82.6000	33.00	5.90
9805773	29.3000	139.0000	424.00	6.20
9815881	−16.2000	−176.3000	364.00	6.10
9815885	−19.5000	169.0000	114.00	6.00
9809277	7.8000	136.8000	33.00	6.10
9809281	14.2000	146.1000	62.00	6.50
9815853	−1.2000	121.3000	33.00	6.10
9811425	−21.8000	−179.5000	579.00	7.40
9811437	−23.8000	178.4000	694.00	7.70
9811933	31.0000	141.9000	10.00	6.20
9814273	43.2000	146.1000	30.00	5.80
13811732	−20.0000	−176.2000	211.00	5.90
13813032	44.9000	130.1000	578.00	6.50
9827425	−31.4000	−68.9000	117.00	6.40
9827509	−10.5000	161.1000	33.00	6.20
9827697	−10.5000	161.0000	33.00	6.20
9827849	−10.6000	161.2000	33.00	6.30
9830809	23.4000	−108.4000	10.00	6.30
9850213	−8.3000	−71.5000	536.00	6.80
9850509	−14.7000	−175.4000	33.00	6.00
9852585	41.3000	142.1000	58.00	6.10
9851361	51.9000	157.3000	102.00	6.20
9851421	−15.7000	−173.0000	33.00	6.30
9851553	−19.7000	−178.6000	589.00	6.20
9852093	44.3000	149.8000	33.00	6.20
9855193	−20.5000	−178.6000	552.00	6.20
9852973	63.6000	−148.0000	10.00	6.70
9856397	38.9000	141.9000	49.00	6.10
9856489	63.7000	−147.7000	10.00	7.90
13911524	48.0000	146.3000	507.00	7.50
13913348	−14.4000	167.8000	33.00	6.80
9871201	−24.1000	179.1000	531.00	6.10
9877157	−20.6000	−177.7000	377.00	6.50
9877713	−33.6000	−69.8000	111.00	6.00
9880477	44.3000	−129.1000	10.00	6.00
9881337	−10.4000	160.7000	33.00	7.50
9881501	13.7000	−90.8000	33.00	6.30
9881693	18.8000	−103.9000	33.00	7.30
9889609	53.5000	−164.6000	3.00	6.50
13947104	−17.3000	−175.3000	275.00	6.10
13948052	51.5000	177.9000	33.00	6.80
13950664	−15.3000	−173.5000	41.00	5.90
13952108	35.3000	−35.6000	10.00	6.10
9906733	7.0000	−82.2000	10.00	6.10
13959288	−20.9000	169.7000	96.00	6.20
13959416	−8.1000	−71.5000	546.00	5.90
13959884	43.7000	147.7000	60.00	6.00
13960816	−15.2000	−173.7000	33.00	6.00
13961036	−30.6000	−178.4000	33.00	6.60
13961120	−30.6000	−178.3000	33.00	6.40
9915333	−17.4000	167.7000	33.00	6.20
9915537	18.2000	−58.7000	40.00	6.60
9916657	−18.0000	−178.8000	564.00	6.00
13967192	38.9000	141.5000	53.00	6.90
13971644	51.7000	176.8000	33.00	6.40
9923497	55.5000	159.9000	173.00	6.30
13973676	−7.5000	−71.6000	553.00	7.10
13973684	−30.5000	−71.4000	37.00	6.80
13973876	51.6000	176.7000	30.00	6.90
9927909	−21.2000	−174.5000	33.00	6.00
9934337	−15.5000	166.2000	33.00	6.00
13980296	38.5000	141.0000	33.00	6.10
13980656	47.2000	139.2000	481.00	6.70
13986572	−45.2000	167.1000	33.00	7.00
9940569	14.1000	−91.1000	117.00	6.00
9942121	43.5000	132.2000	480.00	6.10
9942373	−15.2000	−173.2000	10.00	6.20
13992200	−21.4000	−68.0000	127.00	6.10
13992884	19.9000	95.7000	10.00	6.70
13992964	19.7000	−70.7000	10.00	6.50
13993864	41.8150	143.9100	27.00	8.30
9948765	42.1000	144.5000	33.00	6.00
13994256	50.1000	87.7000	18.00	7.50
13994328	50.1000	87.8000	33.00	6.30
13994580	42.4000	144.4000	33.00	6.50
9948189	−30.4000	−177.4000	33.00	6.30
9948309	50.2000	87.7000	10.00	6.70
9949493	−16.5000	−170.3000	33.00	6.10
9949789	42.6000	144.5000	33.00	6.60
13997908	−5.5000	154.1000	134.00	6.40
14000576	37.9000	142.5000	33.00	6.60
14001772	5.0000	−77.7000	33.00	6.00
14002128	−19.4000	168.9000	112.00	6.60
14003056	22.3000	143.3000	113.00	6.10
14003172	33.6000	137.0000	391.00	6.40
14004236	51.3000	178.6000	33.00	7.80
14007860	55.5000	165.7000	10.00	6.60
9961913	51.5000	−179.3000	53.00	6.00
9968869	8.4000	−82.8000	33.00	6.50
14018688	−34.8000	−178.4000	10.00	6.00
9969201	−22.3000	169.5000	10.00	6.50
9969853	−22.0000	169.6000	10.00	7.00
9970277	−21.8000	169.7000	10.00	6.60
14018788	−22.4000	169.5000	33.00	6.10
14018912	−22.3000	169.6000	10.00	6.40
14024824	−16.7000	−174.2000	134.00	6.60
14027372	8.4000	−83.0000	29.00	6.10
9985713	−14.7000	−175.7000	15.00	6.20
9985929	35.2000	−4.0000	2.00	6.50

Table B1. (*Continued*.)

Event ID	Latitude (°)	Longitude (°)	Depth (km)	M_w
9990429	−15.5000	−175.2000	270.00	6.00
9991793	−21.1000	−65.6000	288.00	6.10
14039076	−23.8000	−176.0000	46.00	6.10
9997129	−20.4000	−173.9000	41.00	6.00
9998493	−13.2000	167.2000	231.00	6.50
9999301	42.9000	144.8000	42.00	6.10
10000249	55.3000	162.6000	65.00	6.20
14049176	−21.9000	−174.9000	10.00	6.00
10005365	−37.6000	−73.2000	30.00	6.60
10006349	−22.0000	170.3000	10.00	6.10
10014157	34.3000	141.3000	38.00	6.60
10014433	−31.1000	−177.1000	57.00	5.90
14061408	−32.9000	−179.5000	43.00	6.20
14064988	55.7000	160.0000	184.00	7.00
14065184	−38.8000	−73.1000	38.00	6.10